Optical fiber Bragg grating-based pressure sensor for soil monitoring applications

Muhammad Syamil Mohd Sa'ad,[a] Harith Ahmad,[a,b,c,*] Mohamad Ashraff Alias,[a] Muhammad Khairol Annuar Zaini,[a] Muhamad Zharif Samion,[a] Kenneth T. V. Grattan,[d] B. M. Azizur Rahman,[d] Gilberto Brambilla,[e] Lim Kok Sing,[a] Sulaiman Wadi Harun,[f] Leonard Bayang,[a] Siti Aisyah Reduan,[a] Kavintheran Thambiratnam,[g] Mohd Zamani Zulkifli,[g] and Mohammad Faizal Ismail[a]

[a]Universiti Malaya, Photonics Research Center, Kuala Lumpur, Malaysia
[b]Universiti Malaya, Department of Physics, Faculty of Science, Kuala Lumpur, Malaysia
[c]Universiti Kuala Lumpur British Malaysian Institute (UniKL BMI), Selangor, Malaysia
[d]City, University of London, School of Mathematics, Computer Science and Engineering, London, United Kingdom
[e]University of Southampton, Optoelectronics Research Center, Southampton, United Kingdom
[f]Universiti Malaya, Department of Electrical Engineering, Faculty of Engineering, Kuala Lumpur, Malaysia
[g]International Islamic University Malaysia, IIUM Photonics and Quantum Centre, Kulliyyah of Science, Jalan Sultan Ahmad Shah, Bandar Indera Mahkota, Pahang Darul Makmur, Malaysia

ABSTRACT. An optical-based pressure sensor for a 150 × 150 mm surface was designed and fabricated. The sensor utilizes a fiber Bragg grating (FBG) attached to a 30 × 30 × 30 mm actuator as the pressure sensing mechanism. The middle section of the actuator, which is circular, can bend into an elliptical form and, in the process, pull the FBGP via both ends when force or pressure is applied, thus converting the pressure applied to its surface into a wavelength shift. In laboratory testing, a sensitivity of 0.152 nm/kPa was obtained. Subsequently, the pressure sensor was tested in the field by burying it 20 cm underground to measure soil pressure, while another FBG was spliced in series to the FBGP to compensate for temperature variations. Testing shows that the proposed design can realize a compact optical-based pressure sensor with enhanced soil monitoring applications such as dynamic soil pressure caused by soil movement.

Keywords: fiber Bragg gratings; fiber Bragg grating sensors; ground movement; soil pressure; pressure sensor

1 Introduction

Accurate and precise information on soil movement at any given time is essential in evaluating and monitoring structural risks and health. In many cases, incidences and disasters pertaining to structural failures occur due to a lack of information on the movement of soil or the changes of pressure exerted onto supporting structures. These changes often exceed the pressure and strain limits of the structure, resulting in failure.[1]

To overcome these challenges, using sensors to monitor soil movement and pressure in structures actively is becoming increasingly commonplace.[2] There are several already commercially

available soil pressure sensors, using either electrical, micro-electro-mechanical systems (MEMS), or piezo ceramic sensing mechanisms.[3–5] Although these sensors can provide soil pressure and movement measurement, they suffer from various limitations that affect their performance. For instance, electrical-based pressure sensors are prone to electromagnetic interference and suffer from a limited monitoring range,[6] whereas MEMS and piezo ceramic sensing mechanisms are highly sensitive but suffer from geometry issues, robustness, and single measurement value.[7,8]

In this regard, optical fiber sensors have become the focus of extensive research efforts to develop a high-potential alternative to the aforementioned sensors. Optical fiber sensors have already demonstrated high sensitivity, accuracy, robustness, and cost effectiveness in sensing applications for temperature,[9] humidity,[10] and pressure.[11–15] Fiber Bragg grating (FBG) based sensors are primarily the most reliable and potential candidates in developing an optical-based soil pressure and movement sensor due to their highly linear response to strain and temperatures. FBG sensors are also advantageous compared with mechanical and electrical base sensors due to their small size and resistance to electromagnetic interference.[16] They are also unique because they have multiplexing capabilities that allow many FBG-based sensors to be spliced into a single fiber,[17] reducing the overall cost of deployment and operation. This provides for cross-sensing applications such as strain and temperature measurement in a single sensor network.[18,19] Many researchers have already demonstrated FBG sensors to measure strain,[20,21] temperature,[22] inclination,[23,24] humidity,[25] and pressure,[26–28] indicating their potential as a sensor.

However, despite the numerous FBG-based pressure sensors demonstrated, only a handful focus on soil condition monitoring applications. For instance, Sheng et al.[26] proposed a simple FBG-based pressure sensor with a sensitivity value of 0.00002 nm/kPa utilizing polymer as the strain-induced mechanism. Similarly, Liu et al.[28] proposed an FBG pressure sensor that relies on the deflection of a thin metal diaphragm and has a resulting sensitivity similar to the sensor proposed by Sheng et al.[26] Some designs use three-dimensional (3D) printing technology, such as that demonstrated by Hong et al.,[29,30] which successfully embedded the FBGs onto a polylactic acid (PLA) material for pressure monitoring purposes. However, none of these works explored the potential for soil monitoring applications, thus indicating the gap between the potential of these sensors and their applications.

This work reports the design, fabrication, and testing of an optical-based pressure sensor utilizing two FBGs to measure pressure and temperature simultaneously. In the sensor's design, it was observed that, in soil pressure monitoring, the most common approach is installing the pressure sensors perpendicular or parallel to the soil surface. Ren et al.[31] provided a clear example of installing the pressure sensors using the parallel approach, while on the other hand, Li et al.[32] proposed a soil pressure sensor based on a dual L-shaped lever with a 0.001 nm/kPa sensitivity. The pressure exerted on the top plate of the sensor transmits directly to the L-shaped levers below, inducing strain on the FBG. Similarly, Correia et al.[33] successfully fabricated a soil pressure sensor with a sensitivity of 0.002 nm/kPa by gluing the FBG onto the diaphragm between two stainless steel covers. The pressure was then exerted onto the top surface, causing the diaphragm to stretch and induce strain on the FBG. However, previous works merely reached the point of laboratory calibrations, and no field testing was carried out. As such, the work presented here also provides additional information obtained from field testing. To achieve this, the sensor was first calibrated in the laboratory using weights and then placed beneath a thin layer of soil to verify the device's functionality. The device yielded a sensitivity value of 0.152 nm/kPa during laboratory calibration, 0.0197 nm/kPa during dry soil and 0.0302 nm/kPa during wet soil testings. As such, the proposed sensor is able to realize a compact, optical-based pressure sensor with high potential for various soil engineering applications.

2 Methodology

2.1 Fabrication of the FBG

In this work, an FBG serves as the primary sensing mechanism for measuring the pressure and movement of the soil. The FBGs were fabricated in-house using the phase mask technique, in which the gratings were inscribed onto a hydrogenated single-mode fiber (SMF) using a Krypton fluoride excimer laser at 248 nm. Any strain or pressure exerted onto the structure of the FBG

changes the grating length, changing the peak reflective wavelength or Bragg wavelength, λ_B. This change is defined as

$$\lambda_B = 2n_{\text{eff}}\Lambda, \tag{1}$$

where n_{eff} is the effective refractive index of the SMF and Λ is the distance between the grating respectively. The Bragg wavelength shifts that are associated with the change of strain, $\Delta\varepsilon$, and temperature, ΔT, are written as

$$\frac{\Delta\lambda_B}{\lambda_B} = (1 - p_{\text{eff}})\Delta\varepsilon + (\alpha + \xi)\Delta T, \tag{2}$$

where p_{eff}, α, and ξ represent the photoelastic, thermal expansion, and thermo-optic coefficients, respectively.

2.2 Calibration of the FBG with Temperature

The proposed sensor uses two FBGs designated as the FBG_P and FBG_T, with Bragg wavelengths of 1533.82 and 1542.53 nm, respectively. FBG_P is used for pressure measurements, and FBG_T is a temperature compensator. Both FBGs were spliced in series. For FBG_T, the shift of the Bragg wavelength, $\Delta\lambda_B$, is obtained theoretically using the general equation of FBG below, which is derived from Eq. (2) by considering the strain parameters to be absent:

$$\frac{\Delta\lambda_B}{\lambda_B} = (\alpha + \xi)\Delta T. \tag{3}$$

By rearranging the above equation, we obtain the wavelength shift associated with the temperature changes using the following expression:

$$\frac{\Delta\lambda_B}{\Delta T} = (\alpha + \xi)\lambda_B. \tag{4}$$

Thus, by substituting the values $0.55 \times 10^{-6}/°\text{C}$ and $8.6 \times 10^{-6}/°\text{C}$ for α and ξ, respectively, the theoretical sensitivity of FBG_T toward temperature at the Bragg wavelength at 1542.53 nm is 0.0140 nm/°C.

Before FBG_P was installed on the 3D-printed actuator, both FBG_P and FBG_T were placed into a water bath to obtain their response and sensitivities against temperature, as shown in Fig. 1(a). The temperature calibration setup after FBG_P was installed on the actuator is shown

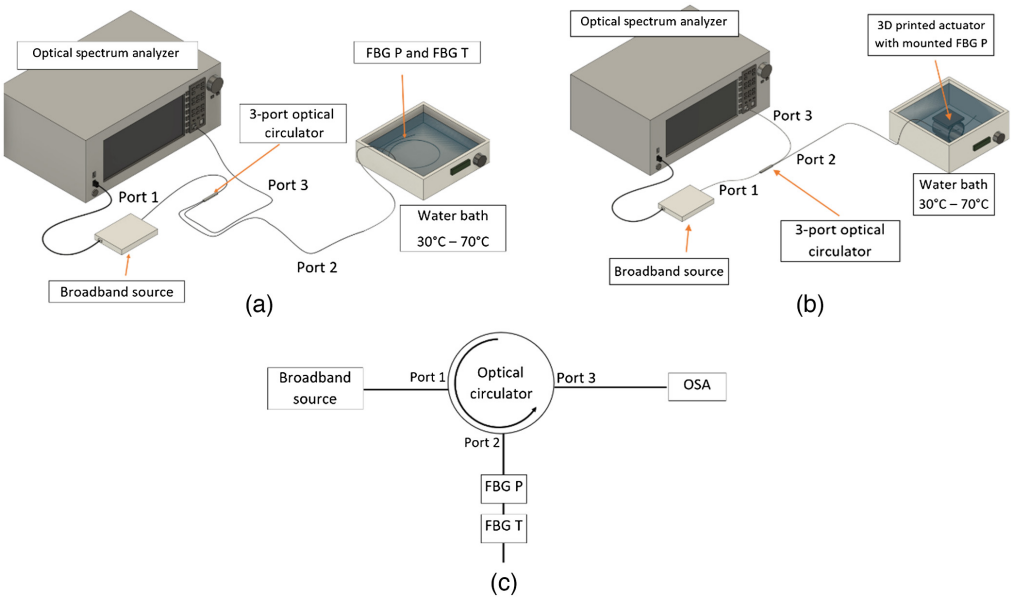

Fig. 1 (a) Temperature calibration setup of bare FBG_P and FBG_T, (b) temperature calibration setup of the FBGs after it was installed on the 3D-printed actuator, and (c) the simplified schematic of the setup.

in Fig. 1(b), and the schematic design of the setup is shown in Fig. 1(c). The single output from the FBGs was connected to port 2 of a three-port circulator, and a broadband source was connected to port 1.

The water bath temperature was increased from 30°C to 70°C in 5°C intervals. This is because Malaysia's ambient temperature does not generally exceed 40°C,[34] and soil temperatures do not fluctuate much compared with the environment temperature.[35] It was reported that the mean annual soil temperature differs from the corresponding air temperature by 3.0 ± 2.1°C. Hence, the sensor is expected to work well within this temperature range.

Port 3 was connected to an optical spectrum analyzer (OSA) with a 0.02 nm resolution and used to take the resulting change in wavelength as the temperature rose. The results of the calibration are discussed in the following sections.

2.3 Fabrication of the Sensor

The actuator prototype has a dimension of $30 \times 30 \times 30$ mm (width × length × height) and was fabricated using a 3D printer, as shown in Fig. 2(a). The 3D printer has a resolution and infill density of 0.1 mm and 5%, respectively. It must be noted that the 3D printer was used only to fabricate the prototype and test the design's working principle.

The actuator was designed with a circular middle section having 2 mm of thickness, followed by square top and bottom parts. The primary function of the circular middle section is to enhance the strain induced onto the FBG as the circular structure pulls both FBG ends simultaneously. This causes considerably more pressure to the FBG than if it was pulled at only one end, thus resulting in more significant wavelength shifts. Because the FBG is directly affected by strain and temperature, the most optimal design for FBG-based sensors is that the actuator must be directly attached to the fiber for the best strain transfer mechanism. This maximizes the sensitivity of the device. By referring to the actuator design in Fig. 2, the FBG is directly attached to the actuator body, indicating that the FBG experiences the most optimum strain transfer mechanism. In addition, the circular middle section makes the actuator easier to compress when vertical pressures are applied because a circular-shaped middle section bends evenly in all directions compared with a segmented-shaped middle section. Therefore, this actuator design is considered practical and feasible to be used as a pressure transducer.

A hole with a diameter of 0.6 mm was created in the middle section to allow the FBG to be inserted. FBG_P was installed on the actuator at the center of the hollow cylinder from one end to the other, as shown in Fig. 2(b). From the front view, the fiber with the FBGs was inserted at one end of the circle going across to the other. The fiber with the FBG was pre-strained before it was

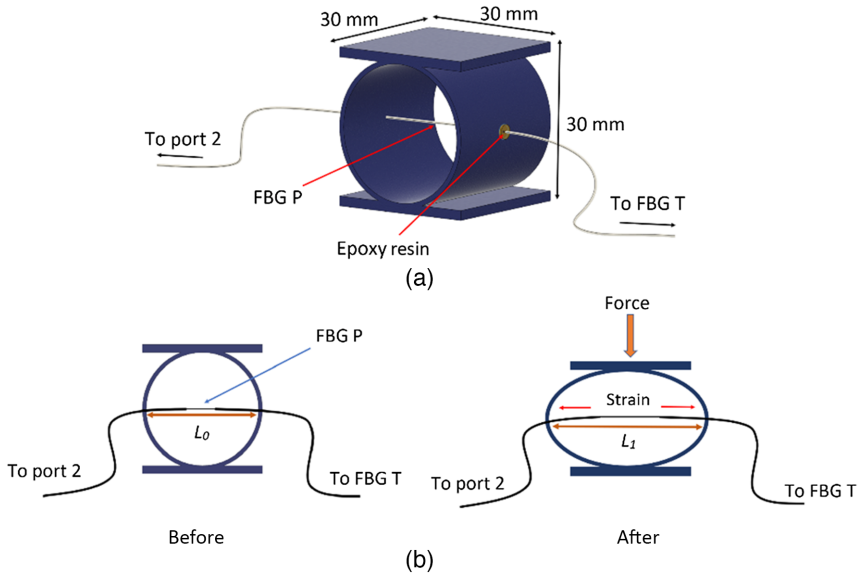

Fig. 2 (a) The installation of FBG_P on the actuator and (b) the side view of the actuator before and after the force was applied, with FBG_P hanging across the middle section.

glued at both ends using epoxy resin to ensure no movement. The diameter of the hole at both ends of the cylinder is about 0.6 mm.

Figure 2(b) shows the side view of the force transfer scheme of the actuator, in which both circular ends pull the FBG_P whenever a force is applied on the top part. The fundamental aspect of this mechanism relates to the linear relationship in the stress versus strain plot, which is given as[36]

$$\sigma = E\varepsilon \text{ or } P = E\varepsilon. \tag{5}$$

Stress, σ, is defined as the force per unit area, which is also known as pressure ($P = F/A$), and strain, ε, is defined as the deformation ratio of a structure from its original length ($\Delta L/L$). The gradient of the linear slope is widely known as Hooke's Law or the modulus of elasticity, E. By referring to the actuator design in Fig. 2 when the actuator was subjected to vertical pressure, P, the relationship between the pressure and the strain, ε_z, is given as[30]

$$\varepsilon_z = \frac{P}{E_z}. \tag{6}$$

Then, the strain due to the vertical pressure was translated into horizontal components, ε_x, which is given as follows:

$$\varepsilon_x = -\upsilon\varepsilon_z, \tag{7}$$

where $-\upsilon$ is Poisson's ratio. By substituting Eq. (6) into Eq. (7), the horizontal strain component is further expressed as

$$\varepsilon_x = -\upsilon\frac{P}{E_z}. \tag{8}.$$

When vertical pressure is applied on top of the actuator, it is essential to note that the horizontal strain component simultaneously acts on the FBG. Thus, the general equation of the FBG as given in Eq. (2) must be included. Because the laboratory calibration was conducted in a temperature-controlled environment, the temperature is considered constant during the experiment, and Eq. (2) is rewritten as

$$\frac{\Delta\lambda_B}{\lambda_B} = (1 - p_{\text{eff}})\varepsilon. \tag{9}$$

As mentioned, because the horizontal strain component also acts on the fiber, Eq. (9) is further expressed as Eq. (10) by substituting the ε_x into the equation:

$$\frac{\Delta\lambda_B}{\lambda_B} = -(1 - p_{\text{eff}})\upsilon\frac{P}{E_z}. \tag{10}$$

Therefore, by rearranging the equation, the magnitude of the applied vertical pressures on top of the actuator, P, is expressed as

$$P = \frac{\Delta\lambda_B E_z}{\upsilon\lambda_B(p_{\text{eff}} - 1)}. \tag{11}.$$

Although the thermal expansion of the PLA can affect the strain measurement, the value is insignificant because the experiment is conducted in the laboratory and in the soil, where the temperature only ranges from 25°C to a maximum of 40°C. It has been observed that the wavelength shift due to the thermal expansion of a material is insignificant at low temperatures compared with the total changes due to the induced strain.[37,38] Hence, to verify whether the coefficient of thermal expansion of the PLA affects the thermal analysis of the FBG, the fabricated actuator with the FBG was placed again in the water bath from 30°C to 50°C as shown in Fig. 1(b) to obtain the thermal response of the FBG after it was mounted to the 3D-printed actuator.

The actuator was then firmly placed and attached to a $150 \times 150 \times 34$ mm waterproof casing made from acrylic. Then, eight actuators were placed without FBGs according to the configuration shown in Fig. 3(a). Such an arrangement ensured that the actuators' bending due to the force applied on top of the sensor was uniform across the effective area. The top cover is directly in contact with the actuator to maximize the effectiveness of the strain transfer from the external

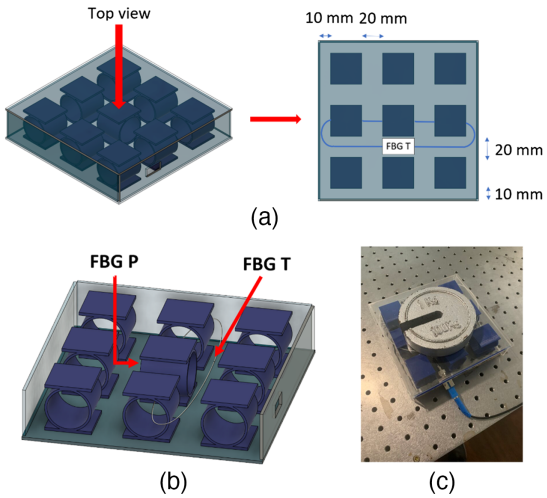

Fig. 3 (a) The actuator configuration inside the casing with top view, (b) an illustration of the device indicating FBG_P, FBG_T positions, and (c) the laboratory calibration procedure of the pressure sensor.

soil to the FBG. This also enables the temperature-induced stress to be effectively distributed to FBG_P if there are temperature variations surrounding the sensor.

As for FBG_T, it was left hanging inside the casing, unattached to any structure, to ensure that it was strain-free. Referring to Fig. 3(b), FBG_T was not mounted inside or onto the actuator but instead was left inside the enclosure, close to FBG_P. This ensures that both FBGs respond similarly to temperature changes and provide a reliable temperature compensation factor for the device. Because FBG_T is strain-free, any wavelength shift at FBG_T indicates a temperature change around the FBGs. Thus, the wavelength shifts of FBG_P need to be offset by the wavelength shift of FBG_T, in which this value then clearly indicates the actual strain it experienced.

2.4 Sensor Calibration in the Laboratory

Initially, a weight of 1 kg was placed directly on top of the sensor, as shown in Fig. 3(c). The weight was then increased in 1 kg intervals until a maximum weight of 10 kg, and its wavelength shift was recorded using the OSA. This procedure was explicitly done to obtain the laboratory calibration data for the pressure sensor. The general equation for pressure, P, as related to force, F, applied to an area of A is as follows:

$$P = \frac{F}{A}. \tag{12}$$

Because force is the mass times the gravitational acceleration, Eq. (3) is rewritten as

$$P = \frac{mg}{A}, \tag{13}$$

where m and g represent mass and gravitational acceleration, respectively. Thus, as per Eq. (11) above, 1 kg weight exerts 0.4 kPa pressure onto a 150×150 mm sensing surface. The procedure was repeated to obtain five different sets of measurements to evaluate the repeatability of the sensor.

2.5 Soil Testing

A $50 \times 175 \times 50$ cm soil container was built to imitate ground structures and soil conditions. The sensor was then buried 20 cm beneath the surface of the soil. Figure 4(a) shows the schematic diagram of the soil container's dimension and the weight placed on the soil surface directly above the pressure sensor. Using the soil volume inside the container of $0.175 m^3$, by $175 \times 50 \times 20$ cm and soil density of $1600\ kg/m^3$, the total calculated weight of the dry soil inside the container is 280 kg. Figure 4(b) shows a diagram of the experimental setup, in which the sensor was laid on the container's floor bed filled with soil. The sensor was connected to a 20 m fiber cable that went straight to the OSA through the optical circulator. A metal rod was placed beside the sensor to

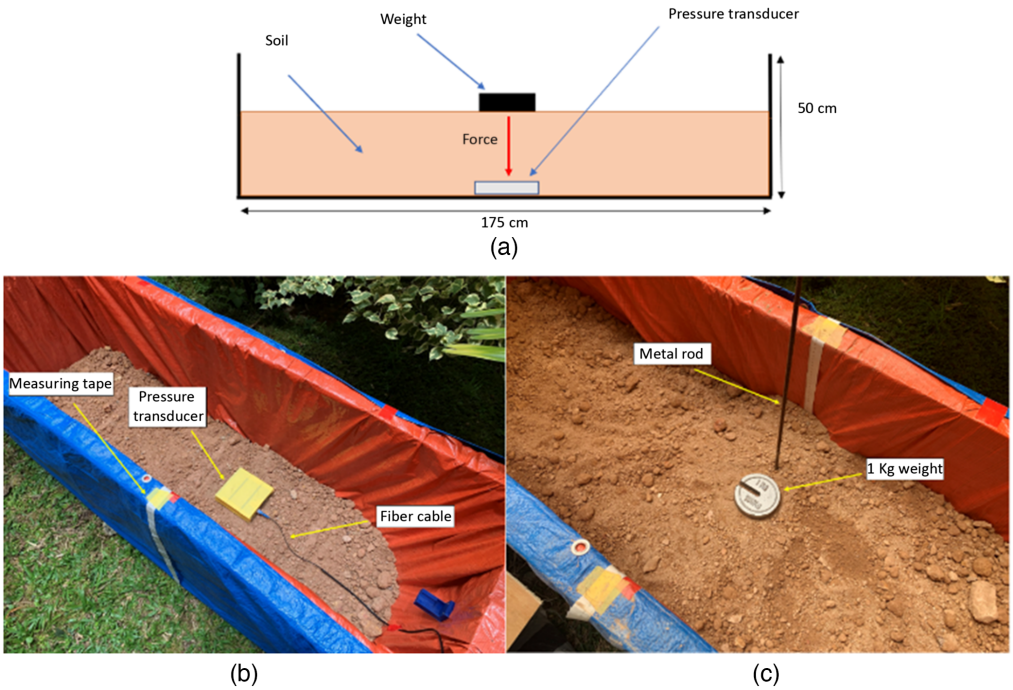

Fig. 4 (a) Illustration of the wooden soil container's dimension (175 cm × 50 cm × 50 cm), (b) the sensor was then placed onto the soil container at about 20 cm below the upper level of the soil, and (c) the placement of the weight above the soil.

determine its exact location when it was already buried in the soil, as shown in Fig. 4(c). A 1 kg weight was placed on top of the soil directly above the device, as shown in Fig. 4(a). The weight was then increased in 1 kg intervals to 10 kg to study the device response inside dry soils. The experiment was repeated with wet soil in which 1 kg of water was poured on top of the soil directly above the sensor.

3 Results and Discussion

The initial spectrum obtained from both FBGs is shown in Fig. 5. Two reflective peaks of 1533.82 and 1542.53 nm are visible, representing the FBG_P and FBG_T, respectively.

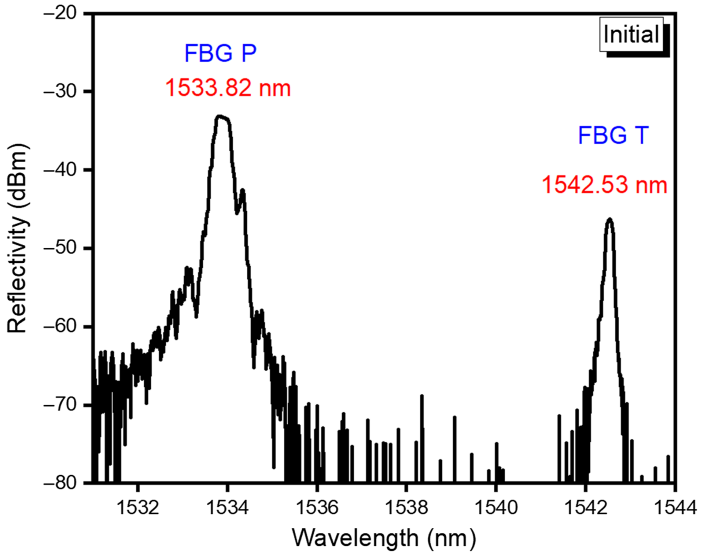

Fig. 5 Initial spectrum for FBG_P and FBG_T at a room temperature of 27.8°C.

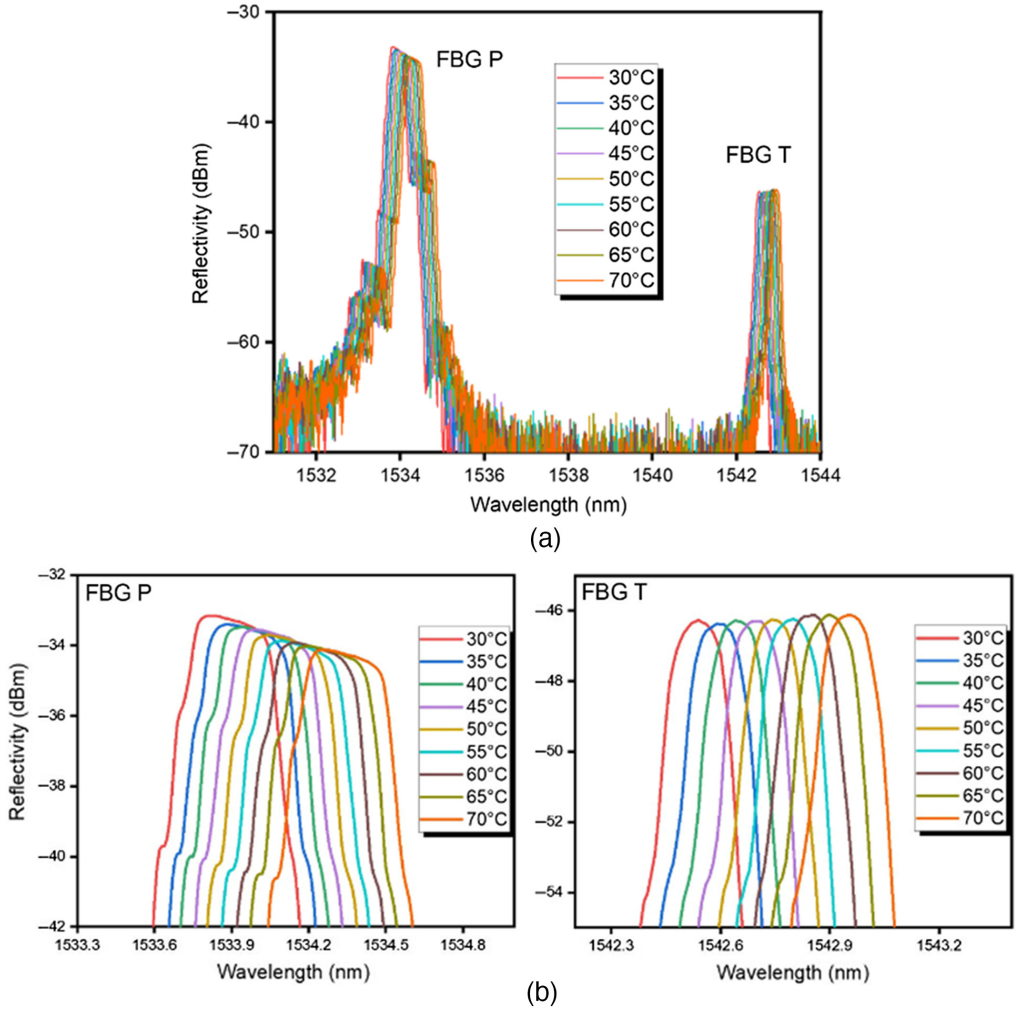

Fig. 6 (a) The spectrum and its (b) closer view for both FBG_P and FBG_T during temperature calibration inside a water bath, from 30°C to 70°C.

Figure 6(a) shows the shifted wavelength spectrum when both FBGs were calibrated for temperature in the water bath setup, and Fig. 6(b) shows a more precise shift of the wavelength spectrum. In Fig. 6(b), more apparent shifts of the reflective peak wavelength for both FBGs can be seen due to the FBG characteristics, which exhibit linear responses toward strain and temperature. The primary purpose of this calibration is to obtain the responsivity values of both FBGs when subjected to different sets of temperatures, so a temperature compensation factor can be considered whenever temperature variations occur.

The graph of the wavelength versus temperature for both the FBG_P and the FBG_T is plotted in Fig. 7. From the plot, both FBGs have an identical linear response of 0.0104 nm/°C toward temperature changes. Because FBG_T was unaffected by the strain, any shifts in the FBG_T reflective peak wavelength indicate temperature variations surrounding the FBG_T, hence providing a temperature compensation factor for the FBG_P. This enables the exact shift due only to strain, not temperature variances.

In addition, Fig. 8 was plotted to show the thermal expansion factor of the FBG when FBG_P was installed on the 3D-printed actuator. For the low-temperature region of 30°C to 50°C, we observe in Fig. 8(a) that FBG_P exhibits a sensitivity value of 0.0106 nm/°C compared with 0.0104 nm/°C in Fig. 7(a). However, in a condition in which the temperature is only in the range of 25°C to 40°C, it has been observed in previous works that the wavelength shift due to the thermal expansion of a material is insignificant at low temperatures compared with the total changes due to the induced strain.[37,38] This is supported in Ref. 37 in which the authors attached both FBG ends to a platinum plate that was heated from room temperature of 25°C up to 400°C.

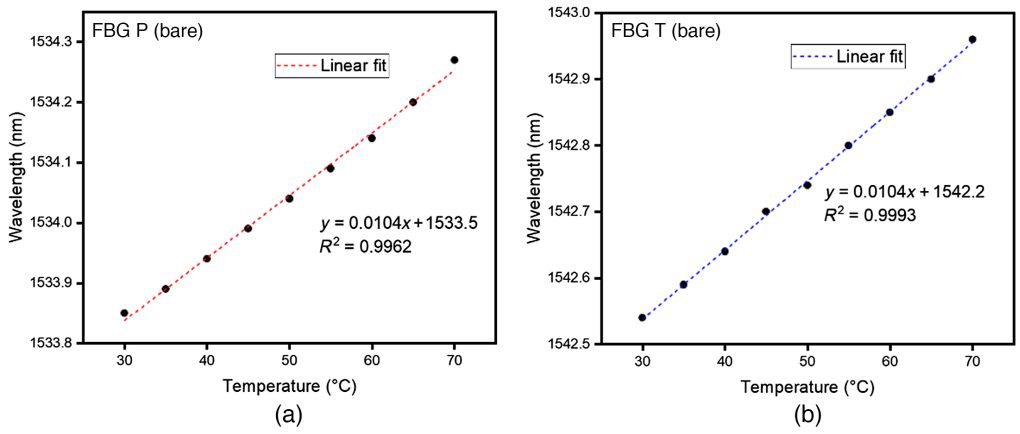

Fig. 7 Wavelength response toward different temperatures for (a) bare FBG_P and (b) bare FBG_T.

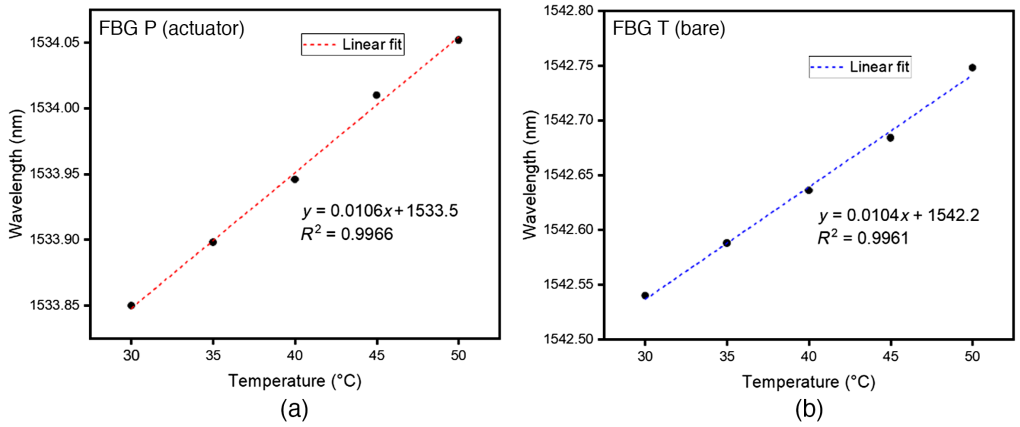

Fig. 8 Wavelength response of (a) FBG_P and (b) FBG_T after installation on the 3D-printed actuator.

The authors found that, at 26°C, the difference in the wavelength shift was only 0.000067 nm, considered small and insignificant compared with the total changes due to induced strain. In fact, up to 40°C, the difference in the shift was lower than 0.0001 nm, so we can neglect the shifts due to the slight temperature change. However, at a high temperature of 400°C, a 0.25 nm difference in the wavelength shift was observed, and this value should then be included in the thermal response analysis of FBG sensors due to a significant difference in the wavelength shift. Because the experiment was conducted in the environment with temperature ranging from 20°C to 40°C, the thermal expansion of PLA can be neglected in the thermal-strain analysis of FBG_P. In addition, a similar linear response is observed in both Figs. 7(b) and 8(b) because, in both cases, FBG_T was left unstrained and unattached to any structure or material.

Figure 9(a) shows the wavelength spectrum when the device was subjected to different weights, exerting vertical pressures on top of it, ranging from 0 to 4.4 kPa. FBG_P exhibits shifts in the wavelength spectrum, whereas FBG_T indicates no change. The constant wavelength spectrum of FBG_T verifies that there are no temperature variations during the experiment and that no temperature compensation is needed for the FBG_P wavelength measurements. The graph of the wavelength response against the weights applied is plotted in Fig. 9(b); we obtained the sensor's sensitivity to be 0.152 nm/kPa. This device yields better sensitivity than previous designs, such as those by Li et al.[32] and Hong et al.,[29] which recorded a sensitivity value of 0.00112 and 0.00007 nm/kPa, respectively. Another significant finding highlighted in the figure is the starting point of the sensor's optimum operating range. In Fig. 9(b), it can be observed that the plot is linear, starting from 0.4 kPa of pressure applied up to 4.4 kPa. Below 0.4 kPa, the sensor exhibits no response because the FBG was initially loose due to fabrication defects.

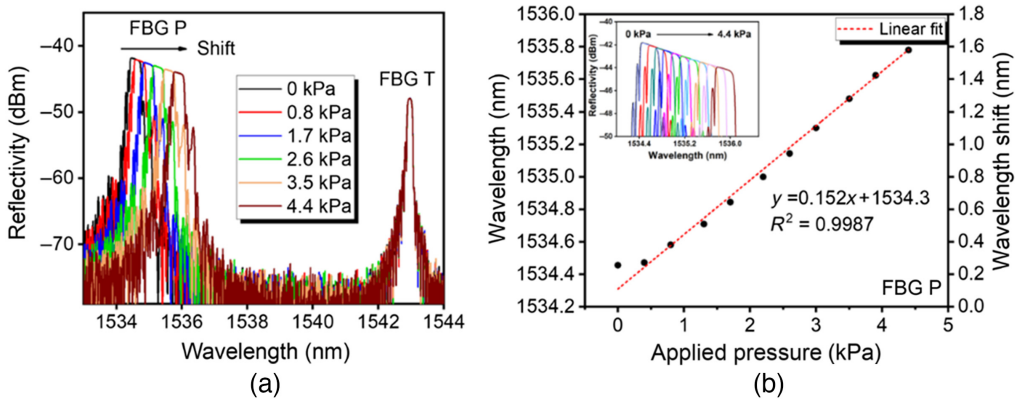

Fig. 9 (a) The wavelength spectra for both FBGs when the sensor was subjected to different pressures and (b) the linear response of the device during the laboratory calibration up to 4.4 kPa with the inset giving clearer wavelength shifts of the reflective peak.

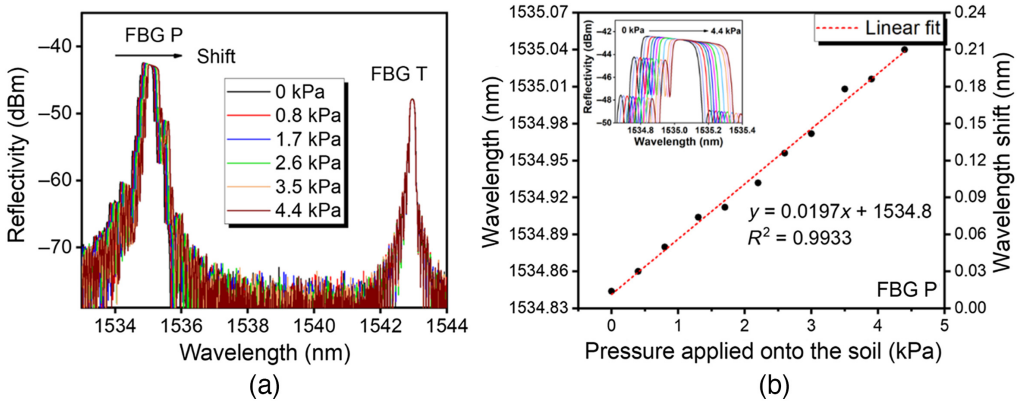

Fig. 10 (a) The wavelength spectra for both FBGs and (b) the linear response of FBG_P with the inset giving more apparent wavelength shifts of the reflective peak when the sensor was subjected to 0 to 4.4 kPa pressures during the dry soil testing.

Figure 10(a) shows the spectrum of the FBGs during the dry soil testing, and from the spectrum itself, it is observed that it exhibits minor wavelength shifts compared with the laboratory calibration spectrum in Fig. 9(a). This is proven in Fig. 10(b), as the plot verifies that the device's response during the dry soil testing yielded a sensitivity value of 0.0197 nm/kPa when pressures were exerted on top of the soil by the weights. The value is lower than the laboratory calibration value by ~7.7 times.

Figure 11(a) shows the wavelength spectrum of both FBG_P and FBG_T during the wet soil testing, and Fig. 11(b) shows the linear response of FBG_P toward applied pressures in wet soil conditions. Figure 11(b) shows that FBG_P yields a more considerable sensitivity value of 0.0302 nm/kPa during the wet soil testing, compared with the dry soil testing value in Fig. 10(b), which is 0.0197 nm/kPa. During the field test, water was poured on top of the soil directly above the sensor to study the sensor's performance in wet soil conditions. The water binds the soil particles together, causing the soil to become more compact, reducing its thickness, and affecting the pressure distribution inside the soil. This resulted in the soil above the sensor becoming denser,[39] and the pressure applied on top of the area became more concentrated compared with the dry soil conditions. The dry soil is less dense than the wet soil; hence, the pressures are more widely distributed.

However, excessive water infiltration causes the loosening of the soil structure with an increased soil permeability.[40] On the other hand, some soils have a high clay content, which means that they can expand significantly when saturated with water. This expansion can cause the soil to push up and outward, increasing its thickness and affecting the pressure distribution inside the soil.

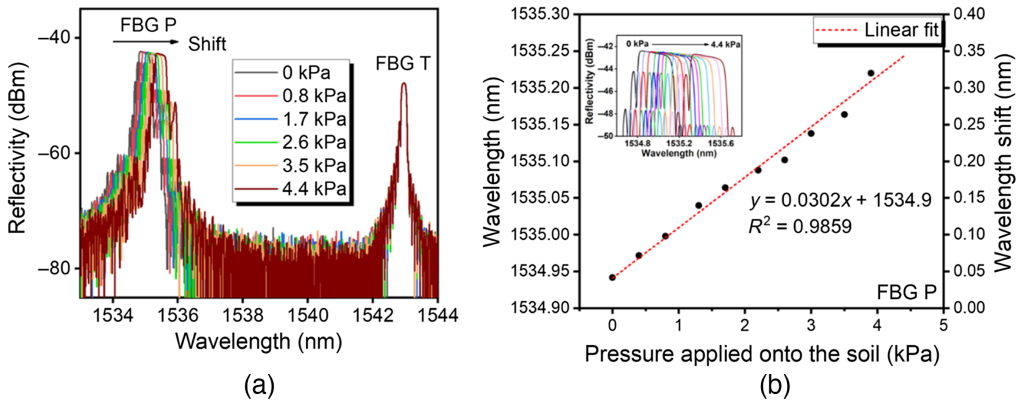

Fig. 11 (a) The wavelength spectra for both FBGs and (b) the linear response of FBG_P with the inset giving more evident wavelength shifts of the reflective peak when the sensor was subjected to 0 to 4.4 kPa pressures during the wet soil testing.

Furthermore, by referring to Figs. 9–11, the different test conditions give different FBG responses toward applied pressure in terms of its sensitivity value. The sensitivity of the dry and wet soils is smaller compared with that in the laboratory condition. This implies that the central pressure disperses from the column to the surrounding soil in the case of dry and wet soils. Therefore, the actual force experienced by the sensor is much less due to the force being transferred and distributed to all directions in the soil, resulting in a lower pressure value if the force is directly applied on top of the sensor, as indicated in the laboratory calibration. However, the highest pressure expected to be applied to the soil is below the weight. The weight of a certain width induces the highest pressure until the depth equals its width.[41,42] In addition, Ref. 43 successfully created a simulation of the soil structure failure analysis of the force distribution caused by weights (footing) that is heavily affected by its width. In addition, Figs. 9(a), 10(a), and Fig. 11(a) did not exhibit any wavelength shift at FBG_T, which proved that there were no temperature variations when the measurements were taken.

Tables 1–3 present the standard deviation of five different pressure measurements of the device during the laboratory calibration, dry soil, and wet soil testings, respectively. The pressures are calculated using a ratio of the laboratory sensitivity value to the actual wavelength shift value acquired during the field test. The sensitivity value obtained in the laboratory is 0.152 nm/1 kPa, which is rewritten as

$$\frac{0.152\ \text{nm}}{1\ \text{kPa}}. \tag{14}$$

Table 1 Standard deviation of five pressure measurements of the sensor when it was subjected to 1.3, 3.0, and 4.4 kPa pressures during laboratory calibration.

Laboratory calibration					
1.3 kPa		3.0 kPa		4.4 kPa	
Measurement	Calculated pressure (kPa)	Measurement	Calculated pressure (kPa)	Measurement	Calculated pressure (kPa)
1	1.293	1	2.980	1	4.413
2	1.319	2	3.006	2	4.387
3	1.267	3	3.030	3	4.361
4	1.293	4	2.980	4	4.440
5	1.319	5	3.006	5	4.387
Standard deviation	0.019	Standard deviation	0.018	Standard deviation	0.027

Table 2 Standard deviation of five pressure measurements obtained from the sensor when 1.3, 3.0, and 4.4 kPa pressures were applied on top of the soil during dry soil testing.

Dry soil testing					
1.3 kPa		3.0 kPa		4.4 kPa	
Measurement	Calculated pressure (kPa)	Measurement	Calculated pressure (kPa)	Measurement	Calculated pressure (kPa)
1	1.916	1	2.111	1	2.306
2	1.898	2	2.103	2	2.366
3	1.942	3	2.133	3	2.344
4	1.938	4	2.099	4	2.331
5	1.944	5	2.089	5	2.288
Standard deviation	0.017	Standard deviation	0.014	Standard deviation	0.028

Table 3 Standard deviation of five pressure measurements obtained from the sensor when 1.3, 3.0, and 4.4 kPa pressures were applied on top of the soil during wet soil testing.

Wet soil testing					
1.3 kPa		3.0 kPa		4.4 kPa	
Measurement	Calculated pressure (kPa)	Measurement	Calculated pressure (kPa)	Measurement	Calculated pressure (kPa)
1	2.352	1	2.633	1	2.990
2	2.338	2	2.652	2	2.999
3	2.388	3	2.674	3	2.992
4	2.377	4	2.649	4	3.008
5	2.372	5	2.628	5	3.005
Standard deviation	0.018	Standard deviation	0.016	Standard deviation	0.022

This expression indicates that, for every 1 kPa of vertical pressure, the FBG wavelength shifts to a longer wavelength with a value of 0.152 nm. During the field test, when a certain amount of vertical pressure, x, was applied, a wavelength shift of $\Delta\lambda_B$ is obtained as follows:

$$\frac{\Delta\lambda_B \text{ nm}}{x \text{ kPa}}. \tag{15}$$

Thus, by relating both equations, the following expression in which x is the pressure to be calculated is obtained:

$$\frac{0.152 \text{ nm}}{1 \text{ kPa}} = \frac{\Delta\lambda_B \text{ nm}}{x \text{ kPa}}. \tag{16}$$

From the tables, it is observed that each measurement indicates a low standard deviation value, which proves the repeatability of the sensor. Table 1 shows that, when 1.3 kPa of pressure was applied on top of the sensor in the laboratory condition, the calculated pressure was nearly similar to the actual pressure. However, in Table 2, when 1.3 kPa of pressure was applied on top of the soil in dry soil conditions, the device recorded a 1.9 kPa of pressure instead of 1.3 kPa. It was due to the additional 7 kg of soil directly above the sensor, which was calculated using the soil density of 1600 kg/m^3 and the soil volume of 0.0045 m^3, which was calculated using

the cross-section area of 15×15 cm^2 and the soil height of 20 cm. Although an applied pressure of 1.3 kPa is expected, it is not equal to the 1.9 kPa recorded in Table 2.

For the dry soil testing, when the applied pressure was 3.0 kPa, the sensor detected around 2.1 kPa. A similar argument can be used as in the first case. This argument can be applied to the next case with a pressure of 4.4 kPa. In addition, this has been explained in Refs. 41 and 42, whereby the measured pressures taken from the wavelength shift gives a value less than the actual applied pressure. It is due to the additional weight distributed across a specific soil volume. A similar discussion can be said for Table 3 in the case of wet soil. For the case of 1.3 kPa, the calculated value is roughly about 2.4 kPa, which is slightly higher by 0.5 kPa. This is due to the extra weight of the water when mixed with the dry soil. Similarly, the same discussion can be applied to the 3.0 and 4.4 kPa of applied pressure.

In addition, for different soil types, it is important to note that sensor recalibration is needed. The sensor needs to be buried with different kinds of soil and tested using the same vertical pressure applied on top of it. Therefore, several sensitivity values can be obtained by plotting the wavelength versus pressure graph for different soil types. Furthermore, in this paper, the sensor was not intended to determine the soil's mechanical properties or even the soil type. Further analysis and data mapping (database) are needed because the value of the vertical pressure alone is insufficient to determine the soil's physical properties. It would be an exciting topic to explore in the future.

4 Conclusion

An optical-based pressure sensor was proposed and demonstrated using FBGs embedded in a novel cantilever design. The sensor utilized an FBG attached to a $30 \times 30 \times 30$ mm actuator as the pressure sensing mechanism. The sensor was initially calibrated in the laboratory, giving a sensitivity of 0.152 nm/kPa, and tested with weights of 1 to 10 kg placed onto it that exerted pressures ranging from 0 to 4.4 kPa. In the actual testing in the field, in which the pressure sensor was placed about 20 cm in dry and wet soil, the device exhibited a reduced sensitivity of 0.0197 and 0.0302 nm/kPa, respectively. The reduced sensitivities were primarily due to the force/pressure from the weight, which was evenly distributed in the soil. A distance of 20 cm between the soil surface and the device significantly reduced the actual pressure experienced by the sensor. The obtained laboratory sensitivity was better, and the sensor performed well. It is evident that using this design and the materials used, the FBGs were very well protected. The proposed design will be suitable for the harsh environment inside soil.

Code, Data, and Materials Availability

The data and materials will be provided upon request. Some materials are not available due to privacy. The authors declare no conflicts of interest.

Acknowledgments

The authors acknowledge the support from the British Council-MIGHT NUOF with Grant No. IF022-2020, Universiti Malaya through Grant Number UM-Innovate PPSI-2020-HICOE-02, RU 005-2021. Professor Ken Grattan also acknowledges support from the Royal Academy of Engineering.

References

1. B. M. Das and K. Sobhan, Principles of Geotechnical Engineering, 8th ed., Cengage Learning (2016).
2. E. Rite, "A guide on geotechnical instruments: types, and application," 2021, https://www.encardio.com/blog/a-guide-on-geotechnical-instruments-types-application (accessed 27 February 2023).
3. Q. Tan et al., "A wireless passive pressure and temperature sensor via a dual LC resonant circuit in harsh environments," *J. Microelectromech. Syst.* **26**(2), 351–356 (2017).
4. Jiakang Electronics, "Piezo ceramic rings /discs-transducers and sensors-products-Zhejiang Jiakang Electronics Co., Ltd.," http://en.jkelec.com/index.php?c=content&a=list&catid=284&gclid=Cj0KCQiAo-yfBhD_ARIsANr56g7pTyAYo2_OgDpZQyYi_gD8IG_jS40oDHHvyr919Y8k5mOrYFctkMoaAspwEALw_wcB (accessed 27 February 2023).

5. Siansonic Technology, "Products," https://www.siansonic.com/Products/Piezo-Ceramic/Standard-Piezo?gclid=Cj0KCQiAo-yfBhD_ARIsANr56g63IjmNjg43FilG02RXv8g2tLf3ji9ThNeB-yub1Dmivil03wWCZUMaAme1EALw_wcB (accessed 27 February 2023).
6. M. Drahansky, Liveness detection in biometrics, in *Advanced Biometric Technologies*, G. Chetty and Y. Jucheng, Eds., InTech, Croatia (2011).
7. H. Pei, J. Yin, and W. Jin, "Development of novel optical fiber sensors for measuring tilts and displacements of geotechnical structures," *Meas. Sci. Technol.* **24**, 095202 (2013).
8. M. Ahmed and M. Meguid, "Patents and techniques of contact pressure measurement in geotechnical engineering," *Recent Patents Eng.* **3**(3), 210–219 (2009).
9. K. S. Lim et al., "Integrated microfibre device for refractive index and temperature sensing," *Sensors* **12**(9), 11782–11789 (2012).
10. W. H. Lim et al., "All-optical graphene oxide humidity sensors," *Sensors* **14**(12), 24329–24337 (2014).
11. W. J. Bock et al., "A photonic crystal fiber sensor for pressure measurements," *Conf. Rec. - IEEE Instrum. Meas. Technol. Conf.* **2**(4), 1177–1181 (2005).
12. T. R. Woliński, A. Jarmolik, and W. J. Bock, "Development of fiber optic liquid crystal sensor for pressure measurement," *IEEE Trans. Instrum. Meas.* **48**(1), 2–6 (1999).
13. W. J. Bock, M. Beaulieu, and A. W. Domanski, "GaAs-based fiber-optic pressure sensor," *IEEE Trans. Instrum. Meas.* **41**(1), 68–71 (1992).
14. C. Zhu et al., "Optical interferometric pressure sensor based on a buckled beam with low-temperature cross-sensitivity," *IEEE Trans. Instrum. Meas.* **67**(4), 950–955 (2018).
15. S. U. Kienitz et al., "Static and dynamic pressure measurement in flight test application with optical Fabry–Pérot sensors," *IEEE Trans. Instrum. Meas.* **70**, 7004611 (2021).
16. A. D. Kersey et al., "Fiber grating sensors," *J. Light. Technol.* **15**(8), 1442–1463 (1997).
17. F. W. D. Pfrimer et al., "A closed-loop interrogation technique for multi-point temperature measurement using fiber Bragg gratings," *J. Light. Technol.* **32**(5), 971–977 (2014).
18. Z. Bo, Y. Gao-shi, and D. Yi-Jun, "Cross-sensitivity of fiber grating sensor measurement," *J. Appl. Opt.* **28**(5), 614–618 (2007).
19. W. Hong-Liang et al., "Study on strain and temperature cross sensitivity of fiber Bragg grating sensor," *J. Appl. Opt.* **29**(5), 804–807 (2008).
20. I.-L. Bundalo et al., "Long-term strain response of polymer optical fiber FBG sensors," *Opt. Mater. Express* **7**(3), 967 (2017).
21. H. L. Liu et al., "Experimental study on an FBG strain sensor," *Opt. Fiber Technol.* **40**(Sept. 2017), 144–151 (2018).
22. C. L. Zhao et al., "A cheap and practical FBG temperature sensor utilizing a long-period grating in a photonic crystal fiber," *Opt. Commun.* **276**(2), 242–245 (2007).
23. N. N. Ismail et al., "Novel 3D-printed biaxial tilt sensor based on fiber Bragg grating sensing approach," *Sens. Actuators, A Phys.* **330**, 112864 (2021).
24. N. N. Ismail et al., "Biaxial 3D-printed inclinometer based on fiber Bragg grating technology," *IEEE Sens. J.* **21**(17), 18815–18822 (2021).
25. G. Woyessa et al., "Temperature insensitive hysteresis free highly sensitive polymer optical fiber Bragg grating humidity sensor," *Opt. Express* **24**(2), 1206 (2016).
26. H. J. Sheng et al., "A lateral pressure sensor using a fiber Bragg grating," *IEEE Photonics Technol. Lett.* **16**(4), 1146–1148 (2004).
27. W. T. Zhang et al., "Ultrathin FBG pressure sensor with enhanced responsivity," *IEEE Photonics Technol. Lett.* **19**(19), 1553–1555 (2007).
28. L. Liu et al., "Temperature-independent FBG pressure sensor with high sensitivity," *Opt. Fiber Technol.* **13**(1), 78–80 (2007).
29. C. Hong, Y. Zhang, and L. Borana, "Design, fabrication and testing of a 3D printed FBG pressure sensor," *IEEE Access* **7**(c), 38577–38583 (2019).
30. C. Hong et al., "A simple FBG pressure sensor fabricated using fused deposition modelling process," *Sens. Actuators, A Phys.* **285**, 269–274 (2019).
31. G. Ren et al., "Research on new FBG soil pressure sensor and its application in engineering," *Optik* **185**(122), 759–771 (2019).
32. F. Li et al., "Fiber Bragg grating soil-pressure sensor based on dual L-shaped levers," *Opt. Eng.* **52**(1), 014403 (2013).
33. R. Correia et al., "Fibre Bragg grating based effective soil pressure sensor for geotechnical applications," *Proc. SPIE* **7503**, 75030F (2009).
34. Malaysian Meteorological Department, "Malaysia's climate," https://www.met.gov.my/en/pendidikan/iklim-malaysia/#Temperaturedistribution (accessed 9 May 2023).
35. J. J. Lembrechts et al., "Global maps of soil temperature," *Global Change Biol.* **28**(9), 3110–3144 (2022).

36. W. C. Young and R. G. Budynas, *Formulas for Stress and Strain*, 7th ed., McGraw-Hill [Journal of the Mechanics and Physics of Solids 3(1)] (1954).
37. S. Prashar, D. Engles, and S. S. Malik, "Effect of thermal expansion mismatch in grating material and host specimen on thermal sensitivity of FBG sensor," *Photonic Network Commun.* **34**(2), 266–270 (2017).
38. G. Hegde, M. V. N. Prasad, and S. Asokan, "Temperature compensated diaphragm based fiber Bragg grating (FBG) sensor for high pressure measurement for space applications," *Microelectron. Eng.* **248**(April), 111615 (2021).
39. G. Rehm, "Understanding the basics of water in soils," 2016, https://agwaterexchange.com/2016/08/14/understanding-the-basics-of-water-in-soils/ (accessed 22 March 2022).
40. C. M. Chan, "Mechanical properties of clayey sand treated with cement-rubbershreds," *Civil Eng. Dimens.* **14**(1), 7–12 (2012).
41. M. Dixit and K. Patil, "Study of effect of different parameters on bearing capacity of soil," in *IGC 2009*, Guntur, India, pp. 682–685 (2009).
42. B. Anderson, "Bearing capacity of soil: why soils matter," 2020, https://www.concretenetwork.com/concrete/footing_fundamentals/why_soils_matter.htm (accessed 22 Oct. 2021).
43. D. V. Griffiths and G. A. Fenton, "Bearing capacity of spatially random soil: the undrained clay Prandtl problem revisited," *Geotechnique* **51**(4), 351–359 (2001).

Muhammad Syamil Mohd Sa'ad received his Bachelor of Science degree (Hons) in pure physics from the Faculty of Science, Universiti Malaya. He is currently a postgraduate student at the Photonics Research Centre, University of Malaya. His research interests focus on fiber optic sensors, mainly on fiber Bragg gratings.

Harith Ahmad received his PhD in laser technology from the University of Wales, Swansea, United Kingdom, in 1983. He is currently a professor in the Department of Physics and director of the Photonics Research Centre, Universiti Malaya, Malaysia. He has been actively pursuing research activities in the field of photonics since 1983. His research interests are in lasers, fiber-based devices for telecommunications, and fiber-based sensors. He is a fellow of the Academy of Sciences, Malaysia.

Mohamad Ashraff Alias received his Bachelor of Science degree (Hons) in industrial physics from the Faculty of Science, Universiti Teknologi Malaysia (UTM) in 2020. He is currently a postgraduate student and a research assistant at the Photonics Research Centre, Universiti Malaya. His current research interests focus on optical fiber sensors, mainly on fiber Bragg gratings.

Muhammad Khairol Annuar Zaini received his bachelor's degree from the Department of Physics, Faculty of Science, University Putra Malaysia, Malaysia, in 2015, and currently is a research officer at Photonics Research Centre, Universiti Malaya. His current research interests include fiber Bragg grating sensors and spatial division multiplexing.

Muhamad Zharif Samion received his bachelor's degree in electrical engineering from the Faculty of Engineering, University of Malaya, in 2015. He is currently pursuing the Doctor of Philosophy (PhD) in photonics engineering in the Photonics Research Centre, University of Malaya. His research focuses on pulsed and multi wavelength fiber lasers.

Kenneth T. V. Grattan received his BSc in physics (first class honors)from Queen's University Belfast in 1974 and his PhD in laser physics. He received his degree of Doctor of Science (DSc) from City University in 1992 for his sensor work. His research interests have expanded to include the development and use of fiber optics and optical systems in the measurement of a range of physical and chemical parameters.

B. M. Azizur Rahman received his BSc Eng and MSc Eng degrees in electrical engineering with distinctions from Bangladesh University of Engineering and Technology, Dhaka, Bangladesh, in 1976 and 1979, respectively. He received his PhD in electronic engineering from University College, London, in 1982. He leads the research group on photonics modeling, specialized in the development and use of the rigorous and full-vectorial numerical approaches, primarily based on the numerically efficient finite element method.

Gilberto Brambilla is a professor at the Optoelectronics Research Centre and, since 2016, has been the co-director and general manager of the Future Photonics Hub. He received his

MSc (Engineering) with honors from Politecnico di Milano, Italy, in 1996 and his PhD in optoelectronics from the University of Southampton in 2002. His research interests include optical fiber sensors, optical fiber structuring using fs lasers, specialty and polymer fibers, new fiber fabrication technologies, and fibers for nuclear sensing.

Lim Kok Sing (M'16) received his BE degree from the Department of Electrical Engineering, Faculty of Engineering, Universiti Malaya, in 2008 and his PhD from the Photonics Research Centre, Universiti Malaya, in 2012. He is currently a senior lecturer in the Photonics Research Centre, University of Malaya. His current research interests include fiber Bragg grating sensors, spatial division multiplexing, and laser medical devices.

Sulaiman Wadi Harun received his bachelor's degree in electrical and electronics system engineering from Nagaoka University of Technology, Japan, in 1996, and his master's and doctoral degrees in photonics technology from the Universiti Malaya in 2001 and 2004, respectively. He has more than 20 years of research experience in the development of optical fiber devices including fiber amplifiers, fiber lasers, and fiber optic sensors.

Leonard Bayang received his BEng degree from the University of Malaya in 2006 and his MEng degree in 2015. He is currently a research officer with Photonic Research Centre, University of Malaya. He has coauthored numerous ISI professional articles and presented his work in many conferences. His current research interests include equipment test and measurement and the development of fast and ultra-fast fiber lasers.

Siti Aisyah Reduan received her Bachelor of Science degree (Hons.) in physics from the Faculty of Science, UTM, Johor, Malaysia, in 2015, and her PhD from the Universiti Malaya in 2020. Her research focuses on pulsed lasers, saturable absorbers, and fluoride fiber-based lasers.

Kavintheran Thambiratnam (member, IEEE) received his BSc and MSc degrees and his PhD in photonics from the University of Malaya, Kuala Lumpur, Malaysia. He has authored more than 50 publications in international journals and conference proceedings. His research interests include fiber amplifiers and fiber-optic sensors, with a particular interest in the applications of optical sensors toward biological applications.

Mohd Zamani Zulkifli received his bachelor's (Hons.) degree in science physics from the University of Malaya in 1999. He then received his Master of Science and PhD from the same university. He is currently an associate professor in the International Islamic University Malaysia. His research primarily involves the fabrication and characterization of rare earth optical fiber preforms.

Mohammad Faizal Ismail received his Bachelor of Engineering (telecommunication) from the Faculty of Engineering, Universiti Malaya in 1999, Master of Engineering (Science) from the Faculty of Engineering, Universiti Malaya in 2004, and PhD in photonics in 2021 from the same university. He is currently a senior research officer in Photonics Research Center, Universiti Malaya, and his research focuses on pulsed, multiwavelength fiber lasers and waveguides.